

MASTER SCIENCE DE LA MATIÈRE
École Normale Supérieure de Lyon
Université de Lyon

Stage 02/05/2021 - 22/07/2021
Corentin PRADOS
M1 Physique

Study of Poiseuille flows adjacent to a corrugated boundary using the domain-remapping method: application to the morphological stability of ice-water interfaces

Abstract :

Near-wall turbulence controls momentum and heat exchanges between a fluid and bounding surfaces. The near-wall turbulence itself depends on the surface topography, which may evolve due to physical processes such as phase changes driven by flows. Hence it is of interest to investigate whether positive feedback between near-wall turbulence and surface dynamics exist, leading to morphological instability and growth of surface textures. Here we investigate the morphological stability of ice-water interfaces using the domain-remapping method. We find that the flow is laminar and the heat flux tends to smooth the topography for Reynolds numbers based on the friction velocity of one hundred and for topography amplitudes less than ten percent of the channel half width. On the contrary, for topography amplitudes greater than ten percent of the channel half width, near-wall turbulence exists and heat fluxes can lead to morphological instability and growth of surface textures.

Key words : *Domain remapping, Poiseuille flow, Boundaries, Heat flux, Shear*

Internship supervised by :

Louis-Alexandre Couston
louis.couston@ens-lyon.fr

ENS de Lyon
Physics Lab
46, allée d'Italie
F-69364 LYON CEDEX 07, FRANCE
<http://www.ens-lyon.fr/PHYSIQUE>



Acknowledgement

I would like to warmly thank Louis-Alexandre Couston for offering me this internship and for following, helping and advising me during these three months. He passed on much knowledge to me and taught me a lot while being very friendly, I am very grateful to him. I would also like to thank the physics laboratory for welcoming me as well as the PSMN team for allowing me to use their calculators.

Contents

Abstract	1
Acknowledgement	2
Introduction	3
1 Poiseuille flow dynamics in plane channel	5
1.1 Model	5
1.2 Steady state	8
1.3 Bifurcation diagrams	10
2 Poiseuille flow dynamics in a channel with a wavy boundary	12
2.1 Model	12
2.2 Influence of topography	15
Bibliography	21
A Appendix	22
A.1 Zero-divergence white noise	22
A.2 Resolution parameters	22
A.3 Domain Remapping Optimisation	23
A.4 Decomposition test	23
A.5 Asymptotic expansion of the boundary condition	24
A.6 Importance of checking	24

Introduction

Ice melting is one of the critical consequences of global warming, in particular through its impact on rising sea levels (Pritchard *et al.* 2012 [15]; Rignot *et al.* 2013 [16]; Kennicutt 2019 [12]). The understanding of this phenomenon by the scientific community is of paramount importance in order to prevent or limit its impact. We can notably see the importance of this melting at the North Pole on the NASA satellite image (**FIGURE 1A**) with the difference in the amount of ice at the North Pole between September 1984 and September 2016 as there is far less ice in 2016 than in 1984. Icebergs, ice shelves and sea ice are kilometre-scale objects whose evolution are controlled by interface melting. This interface can vary rapidly, up to several meters horizontally in one day, as recently observed by Sutherland *et al.* (Sutherland *et al.* 2019 [17]). Therefore it is essential to understand the physics governing this water-ice interface. We will focus in this paper on the turbulence near a corrugated ice-water interface in particular.

Observations of the water-ice interface in nature have revealed a particular topography taking the form of wave patterns. These patterns are called “scallops” (e.g. Carey 1966 [3]; Curl 1966 [6]; Blumberg & Curl 1974 [1]; Thomas 1979 [18]; Gilpin; Hirata & Cheng 1980 [8]; Hanratty 1981 [9]; Nelson; McLean & Wolfe 1993 [13]; Wykes *et al.* 2018 [19]). These are structures of the order of ten centimetres which repeat with a wavelength of the order of ten centimetres too. We can see their shapes on the photo of **FIGURE 1B** where the wavelength of the pattern is of the order of 10 cm. Mitchell Bushuk and his team have experimentally demonstrated this scallop topography of the water-ice interface. They have shown that, under specific experimental conditions, the ice-water interface goes through three regimes: (1) a scallop development regime in which melt rates are highest in scallop troughs, acting to amplify existing perturbations in the ice surface; (2) a scallop adjustment regime with highest melt rates over scallop crests, acting to dampen existing perturbations; and (3) an equilibrium scallop regime in which melt rates maintain a fixed scallop geometry which migrates downstream over time. (Bushuk 2019 [2]). This topography is of great importance on ice melting, indeed the average melting rate can be at least doubled in a scallops topography compared to a flat one. (Bushuk 2019 [2])

The water-ice system is not the only system to form particular periodic topographies. Actually, this is also the case at the interface between a fluid and a granular material such as sand. In this case the wavelength of the repeated pattern can vary from the order of a centimetre, observed on the seabed, to several kilometres, such as dunes in deserts. The shearing of the fluid at the interface mainly governs these morphologies (Charru 2013 [4]). The problems of morphological instabilities at solid fluid interfaces triggered mathematical developments (Hanratty 1981 [9]), subsequently verified experimentally, but not demonstrated numerically in the transient regime, a regime between the laminar regime and the turbulent regime in which we cannot make an asymptotic derivation as shown by François Charru and his team in the case of sand ripples and dunes (Charru 2013 [4]). It turns out that the morphological stability arises in this transient regime, which is why it would be very important to test it numerically. For now we only have a phenomenological explanation for the morphological instability found experimentally in the transient regime. This internship studies this problem, with the aim of answering the question: Is morphological instability possible at the water-ice interface and what is the effect of the control parameters on its evolution? For this, we use a simplified model of topography formation which can be formalised mathematically like this (Hanratty 1981 [9], Couston 2021 [5])

$$\frac{dl(t)}{dt} = q_{\text{water}} - q_{\text{ice}} \quad (1)$$

with $l(t)$ the thickness of the ice, q_{water} the input heat flux from the fluid and q_{ice} the heat flux at the ice top. This formalism has been particularly discussed in the phase change, dissolution and granular material communities. During this internship, we did not include the variation thickness of the ice, we only looked at the input heat flux from the fluid in order to see if a morphological instability was possible at the water-ice interface. Indeed, we hypothesise that a morphological instability is possible if a pre-existing topography forces the flow to provide excess heat where the ice is already thinnest. This hypothesis greatly simplifies the problem as it allows us to discard phase changes (or boundary dynamics more generally) by considering time-invariant topography.

This internship can be seen as the continuation of the work of Louis-Alexandre Couston *et al.* (Couston 2021 [5]). They have already been able to show, with the phase-field method in 3D, the emergence of particular topography dominated by keels and channels that are aligned with the direction of the mean flow (**FIGURE 1C**), as well as their evolution according to the stability of the flow. However, due to numerical constraints, they could not go into the range of control parameters necessary to reach the possibility of emergence of scallops. Indeed, this would require high control parameters unattainable by the phase-field method with the current computational capabilities. This internship is a draft solution test to circumvent these problems by using the

domain remapping method. This method will help to go from a complicated and irregular domain to a simple and flat domain by modifying the basic equations with a coordinate change.

We take the Poiseuille flow as a canonical flow and we limit ourselves for simplicity to 2D flows. This system will be coded in python using the *Dedalus* framework package. *Dedalus* is a differential equation solver using spectral methods. It is written in python and is particularly designed for studies of fluid mechanics with explicit boundary conditions and explicit initial conditions. This report will study the case of the Poiseuille plane without topography at first, then we will study the effects of topography, with a sweep in topography amplitude and flow intensity.

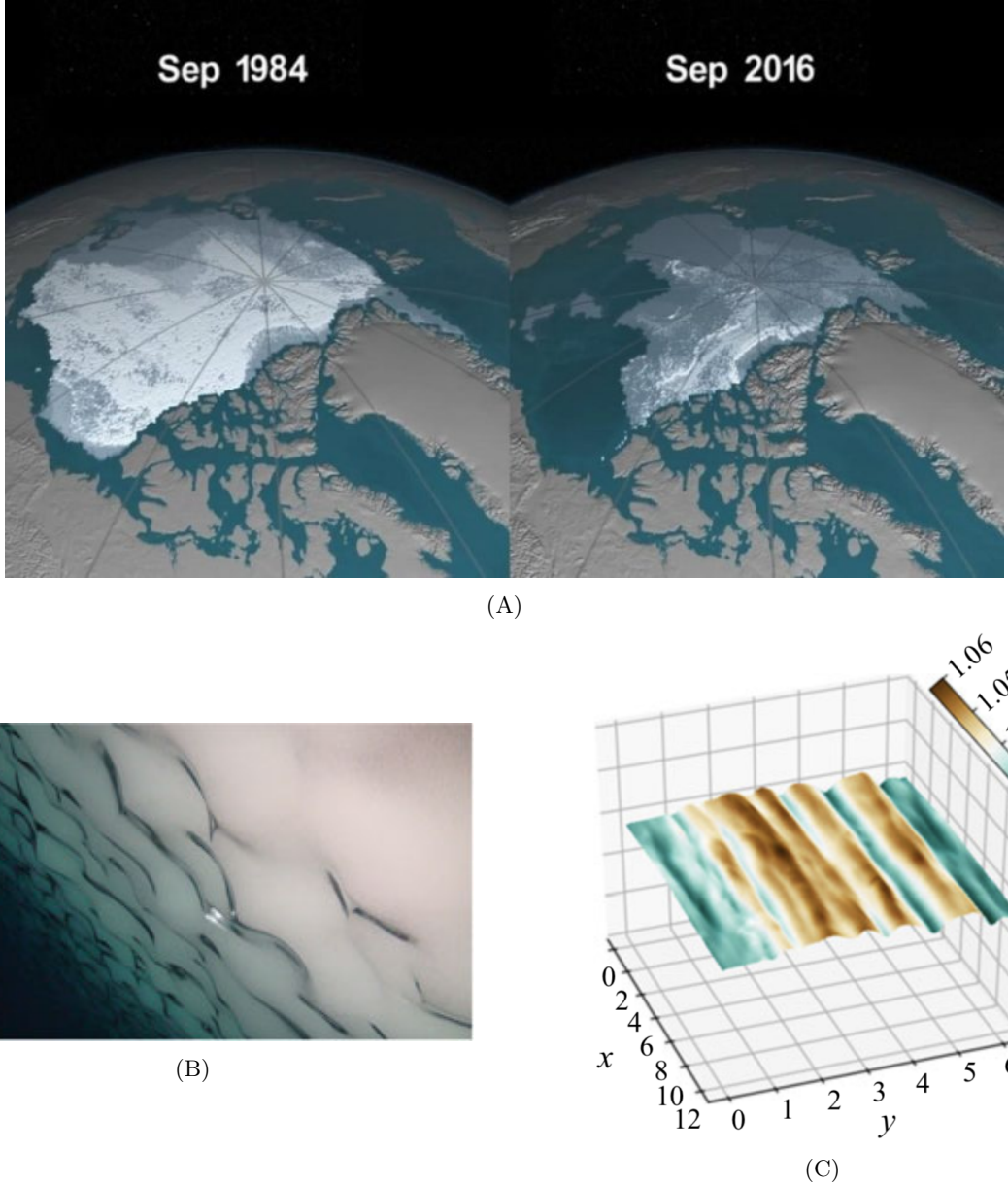


Figure 1: (A) *Difference in the amount of ice at the North Pole between September 1984 and September 2016, Goddard Space Flight Center (NASA)* (B) *Photos of scallop formations on the sides of icebergs taken in the Southern Ocean with a remotely operated vehicle (Hobson, Sherman & McGill 2011 [10])* (C) *Interface topography between a fluid and a solid, channels in the ice are highlighted in brown while keels are highlighted in green. They follow the flow direction which is along to x (Couston 2021 [5]).*

1 Poiseuille flow dynamics in plane channel

The objective of this first study is to become familiar with the Poiseuille flow which will serve as a basis for the study of non-plane boundary conditions. It also provides checks of the efficiency of our programs as the Poiseuille flow is already a well-known flow in the literature. Therefore, we study the properties of a simple Poiseuille flow, *i.e.* in the case where the flow is bounded by two fixed flat plates. We study in particular the properties of the statistically-equilibrated flow when increasing the Reynolds number, which is the main control parameter.

1.1 Model

System

We consider a classical Poiseuille flow, composed of two fixed plates at h and at $-h$. Those plates are of length $L = 8h$, giving an aspect ratio of 4 between length and width. In the channel, the fluid flows at the speed \underline{u} , due to a pressure difference $\Pi = \frac{P_i - P_o}{L} > 0$ (imposed pressure-gradient force), where P_i is the pressure of the inlet of the channel and P_o the pressure of the outlet of the channel with $P_i > P_o$. We also impose a temperature T_b at the bottom and T_t at the top of the channel. We note T the fluid temperature, p the fluid pressure, ρ the fluid density, k the fluid thermal conductivity, c_p the fluid specific heat capacity and η the fluid dynamic viscosity. We define a Cartesian coordinate system (x, z) centred on the bottom of the channel with the z -axis vertically upward, *i.e.* opposite to gravity. [FIGURE 1.1](#) shows our problem schematic.

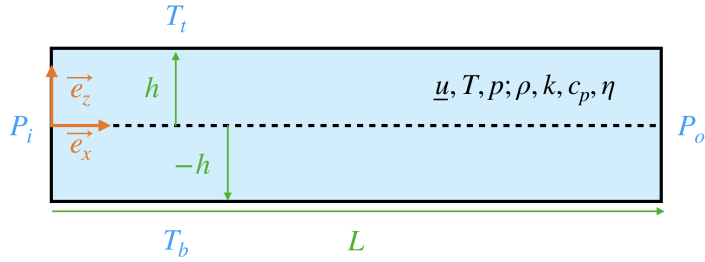


Figure 1.1: Schematic of the Poiseuille flow in plane channel system.

Equations

We consider a generic linear equation of state for the fluid, with the density ρ related to temperature T through

$$\rho = \rho_f(1 - \alpha T) \quad (1.1)$$

with α the thermal expansion coefficient and ρ_f the reference density. The fluid velocity $\underline{u} = (u, w)$ and pressure p evolve according to the mass conservation ([equation \(1.2a\)](#)) and the Navier–Stokes equations ([equation \(1.2b\)](#)) under the Boussinesq approximation. The fluid temperature T evolves according to the energy equation ([equation \(1.2c\)](#)).

$$\nabla \cdot \underline{u} = 0 \quad (1.2a)$$

$$\rho_f(\partial_t \underline{u} + \underline{u} \cdot \nabla \underline{u}) = -\nabla P + \eta \Delta \underline{u} + \Pi e_x + \rho_f \alpha g T e_z \quad (1.2b)$$

$$\partial_t T + \underline{u} \cdot \nabla T = \kappa \Delta T \quad (1.2c)$$

with g the gravitational acceleration and $\kappa = \frac{k}{\rho_f c_p}$.

No-slip boundary conditions impose zero velocity at the wall and we impose a temperature T_b at the bottom and T_t at the top of the channel, leading to

$$\begin{aligned} \underline{u}(z = -h) &= 0, & \underline{u}(z = h) &= 0 \\ T(z = -h) &= T_b, & T(z = h) &= T_t \end{aligned} \quad \begin{aligned} && (1.3\text{a-b}) \\ && (1.3\text{c-d}) \end{aligned}$$

Stationary solution

It can be shown by symmetry and invariance properties that the stationary solution of the problem is the following

$$u_p = \frac{\Pi}{2\eta}(h^2 - z^2) \quad (1.4\text{a})$$

$$w_p = 0 \quad (1.4\text{b})$$

$$T_p = \frac{\Delta T}{2} \frac{z}{h} + \frac{T_t + T_b}{2}. \quad (1.4\text{c})$$

This solution will be used all along this report as a reference.

Dimensionless equations

Let us define the shear τ

$$\tau = \eta \partial_z u. \quad (1.5)$$

The wall shear τ_w is directly proportional to the imposed pressure gradient when applied to the stationary solution of [equation \(1.4a\)](#). It is used for non-dimensionalization,

$$\tau_w = \Pi h \quad (1.6)$$

from which we define the shear velocity u_τ (Zonta & Soldati 2018 [21]) by

$$u_\tau = \sqrt{\frac{\tau_w}{\rho_f}}. \quad (1.7)$$

Using this shear velocity, we define dimensionless variables, denoted by tildes, as

$$\underline{u} = u_\tau \tilde{u}, \quad x = h\tilde{x}, \quad z = h\tilde{z}, \quad t = \frac{h}{u_\tau} \tilde{t}, \quad p = \rho_f u_\tau^2 \tilde{p}, \quad T = \Delta T \tilde{T} \quad (1.8\text{a-g})$$

with $\Delta T = T_b - T_t$ ($T_b > T_t$).

Substituting [equations \(1.8\)](#) into [equations \(1.2\)](#) and [\(1.3\)](#), we obtain the dimensionless equations

$$\tilde{\nabla} \cdot \tilde{\underline{u}} = 0 \quad (1.9\text{a})$$

$$\partial_{\tilde{t}} \tilde{\underline{u}} + \tilde{\underline{u}} \cdot \tilde{\nabla} \tilde{\underline{u}} = -\tilde{\nabla} \tilde{P} + \frac{1}{Re_\tau} \tilde{\Delta} \tilde{\underline{u}} + \underline{e}_x - \frac{Ri_\tau}{2} \tilde{T} \underline{e}_z \quad (1.9\text{b})$$

$$\partial_{\tilde{t}} \tilde{T} + \tilde{\underline{u}} \cdot \tilde{\nabla} \tilde{T} = \frac{1}{Re_\tau Pr} \tilde{\Delta} \tilde{T} \quad (1.9\text{c})$$

$$\tilde{\underline{u}}(\tilde{z} = -1) = 0 \quad (1.9\text{d})$$

$$\tilde{\underline{u}}(\tilde{z} = 1) = 0 \quad (1.9\text{e})$$

$$\tilde{T}(\tilde{z} = -1) = \frac{T_b}{\Delta T} \quad (1.9\text{f})$$

$$\tilde{T}(\tilde{z} = 1) = \frac{T_t}{\Delta T}. \quad (1.9\text{g})$$

The control parameters in [equations \(1.9\)](#) are the Prandtl number, Pr , which compares kinematic viscosity to thermal diffusivity, the friction Reynolds number, Re_τ , which compares the pressure-gradient force to viscous dissipation and the Richardson number, Ri_τ , which compares buoyancy forces to flow shear. They are related to the physical parameters through

$$Pr = \frac{\nu}{\kappa}, \quad Re_\tau = \frac{\rho_f u_\tau h}{\eta}, \quad Ri_\tau = -\frac{2\rho_f \alpha g \Delta T}{\Pi}. \quad (1.10a-c)$$

In a classical ocean-ice system, the Prandtl number is more about $Pr \simeq 10$. However because of numerical constraints, here we fix it to $Pr = 1$. The friction Reynolds number, Re_τ is the control parameter that we will vary. The Richardson number is fixed to zero, $Ri_\tau = 0$. In oceanography, the expression of Richardson is often given by :

$$Ri_\tau = \frac{N^2}{(\partial_z u_\tau)^2} \quad (1.11)$$

with N is the Brunt-Väisälä frequency, corresponding to a measure of stability of a fluid to vertical displacements ([Vallis & Geoffrey K 2017 \[20\]](#)). Therefore fixing $Ri_\tau = 0$ is the same as considering the limiting case of shear-dominated flow, wherein buoyancy effects are negligible.

From this non-dimensional system, the stationary solution can be rewritten, in dimensionless form,

$$\tilde{u}_p = \frac{Re_\tau}{2}(1 - \tilde{z}^2) \quad (1.12a)$$

$$\tilde{w}_p = 0 \quad (1.12b)$$

$$\tilde{T}_p = \frac{1}{2}\tilde{z} + \frac{T_t + T_b}{2\Delta T}. \quad (1.12c)$$

Variables of interest

We define the following rate of flow averaged in x in 2D by:

$$D(t) = <\int_{-1}^1 \tilde{u} d\tilde{z}>_{\tilde{x}}. \quad (1.13)$$

Applying it to the dimensionless stationary state, we get

$$D_p(t) = \frac{2}{3}Re_\tau. \quad (1.14)$$

Then, we define our **first variable of interest** $\mathcal{D}(t)$ corresponding to the following rate of flow averaged in x in 2D scaled by that of the stationary state:

$$\mathcal{D}(t) = \frac{D(t)}{D_p(t)}. \quad (1.15)$$

We use $\mathcal{D}(t)$ to define our **second variable of interest** $\bar{\mathcal{D}}$ corresponding to its averaged according to t :

$$\bar{\mathcal{D}} = <\mathcal{D}(t)>_t. \quad (1.16)$$

Now, we define the heat flux $\Phi_w(t)$ of the flow at the top wall averaged in x , by:

$$\Phi_w(t) = <-k\partial_z T(z = h)>_x. \quad (1.17)$$

Applying it to the dimensionless stationary state, we get

$$\Phi_{w_p} = -\frac{k}{2}. \quad (1.18)$$

Then, we define the Nusselt Nu , our **third variable of interest**, corresponding to the ratio between the heat flux of the flow at the top wall averaged in x and that of the stationary state:

$$Nu(t) = \frac{\Phi_w}{\Phi_{w_p}}. \quad (1.19)$$

We use $Nu(t)$ to define our **fourth variable of interest** \overline{Nu} corresponding to its averaged according to t :

$$\overline{Nu} = \langle Nu(t) \rangle_t. \quad (1.20)$$

1.2 Steady state

Previous works (Falkovitch 2018 [7]) have shown that for every Reynolds number the flow reaches at the end of a certain time a steady state, *ie* a regime either stationary, *ie* time independent, or statistically steady, *ie* we have a particular pattern that repeats itself overtime.

Objectives and problem parameters

We study this stationary state qualitatively using simulation images. To that end, we will plot the dimensionless temperature \tilde{T} , the dimensionless horizontal speed \tilde{u} and the dimensionless vertical speed \tilde{w} at different dimensionless time \tilde{t} in order to look for a steady state. It should also be possible to identify it quantitatively in our simulations by studying $D(t)$ and $Nu(t)$. The principle being that if a steady state is reached, these two variables should, from t_p which defines the start of the statistically-steady state, either do not vary anymore (stationary state) or oscillate around an average value that no longer varies over time (statistically steady state).

We solve numerically the dimensionless [equations \(1.9\)](#). We start each simulation from a superposition of the stationary Poiseuille state of [equations \(1.12\)](#), and a white noise with zero-divergence (see [APPENDIX A.1](#)). For the resolution parameters, we made the choice to settle the *RK222* timestepper and a safety parameter of the CFL of 0.1. The timestepper is the algorithm used to time integrate the solution forward. The safety parameter is a prefactor multiplying the time step calculated via the CFL condition, which is typically smaller than one thus reducing the time step and stabilising time integration. For the spatial resolution, which corresponds to the number of points that we take spatially to solve our problem, we choose $N_x = 512$ in the e_x direction with the *RealFourier* discretization method of *Dedalus*. In the e_z direction, we choose a resolution $N_z = N_x/2 = 256$ with the *ChebyshevT* discretization method of *Dedalus* (see [APPENDIX A.2](#)).

Results

We carried out these simulations for $Re_\tau \in \{10, 30, 50, 70, 90, 100, 107, 108, 110, 120, 125, 130, 140, 150, 152, 155, 160, 165, 170, 175, 200, 250, 300, 400, 500, 600\}$. We will study in this part $Re_\tau = 100$ and $Re_\tau = 200$ in particular. The frames for $Re_\tau = 100$ and $Re_\tau = 200$ can be found respectively [FIGURES 1.2](#) and [1.3](#). We show the temporal evolution of the case $Re_\tau = 100$ through 3 snapshots obtained at different times. After being destabilised by a white noise ([FIGURE 1.2A](#)), the flow goes trough a transitory state ([FIGURE 1.2B](#)) that reverts back to the stationary state alone ([FIGURE 1.2C](#)). Then, we show the temporal evolution of the case $Re_\tau = 200$ through 6 snapshots obtained at different times. After being destabilised by a white noise ([FIGURE 1.3A](#)), the flow goes trough a transitory state ([FIGURE 1.3B](#)) that ends in a meta-stable state ([FIGURE 1.3C](#)). At some point this meta-stable state loses his stability ([FIGURE 1.3D](#)) and transits slowly, in contrast to the first transition, ([FIGURE 1.3E](#)) to a permanent state ([FIGURE 1.3F](#)).

This qualitative description is made quantitative with the time evolution of $D(t)$ and $Nu(t)$ shown in [FIGURES 1.4](#) for $Re_\tau = 100$ and $Re_\tau = 200$. We can see that after a relatively strong transient, the variables stabilise at fixed values. For $Re_\tau = 100$ ([FIGURES 1.4A](#)), we can see that the $D(t)$ and $Nu(t)$ reach exactly the values of one, *ie* the stationary state value. On the contrary, for $Re_\tau = 200$ ([FIGURES 1.4B](#)), $D(t)$ drops to a lower value around 0.4 and $Nu(t)$ rises to a higher value around 4.

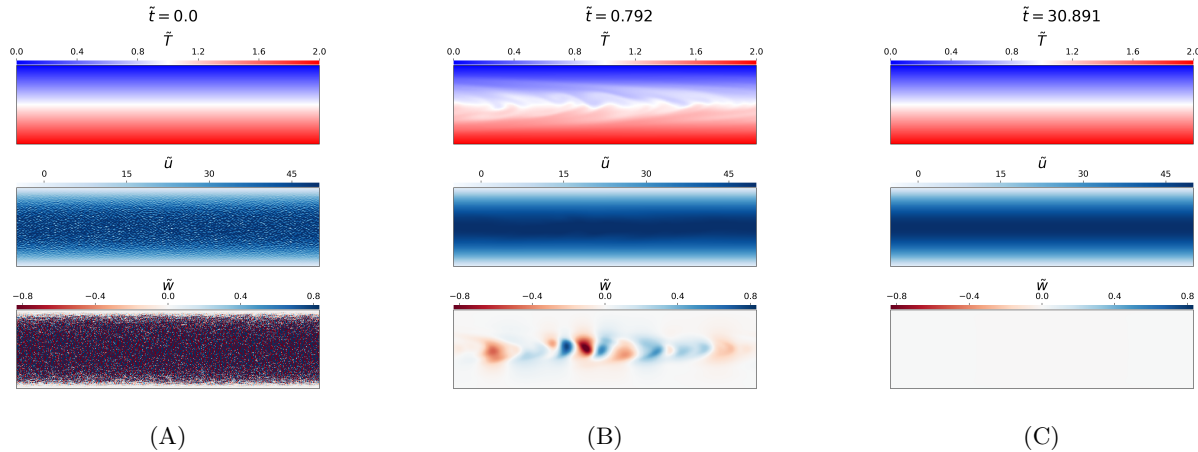


Figure 1.2: Simulation for $Re_\tau = 100$, dimensionless temperature \tilde{T} , dimensionless horizontal velocity \tilde{u} and dimensionless vertical velocity \tilde{w} for different dimensionless time \tilde{t} : (A) Initial state with white noise. (B) Transitory state. (C) Stationary state.

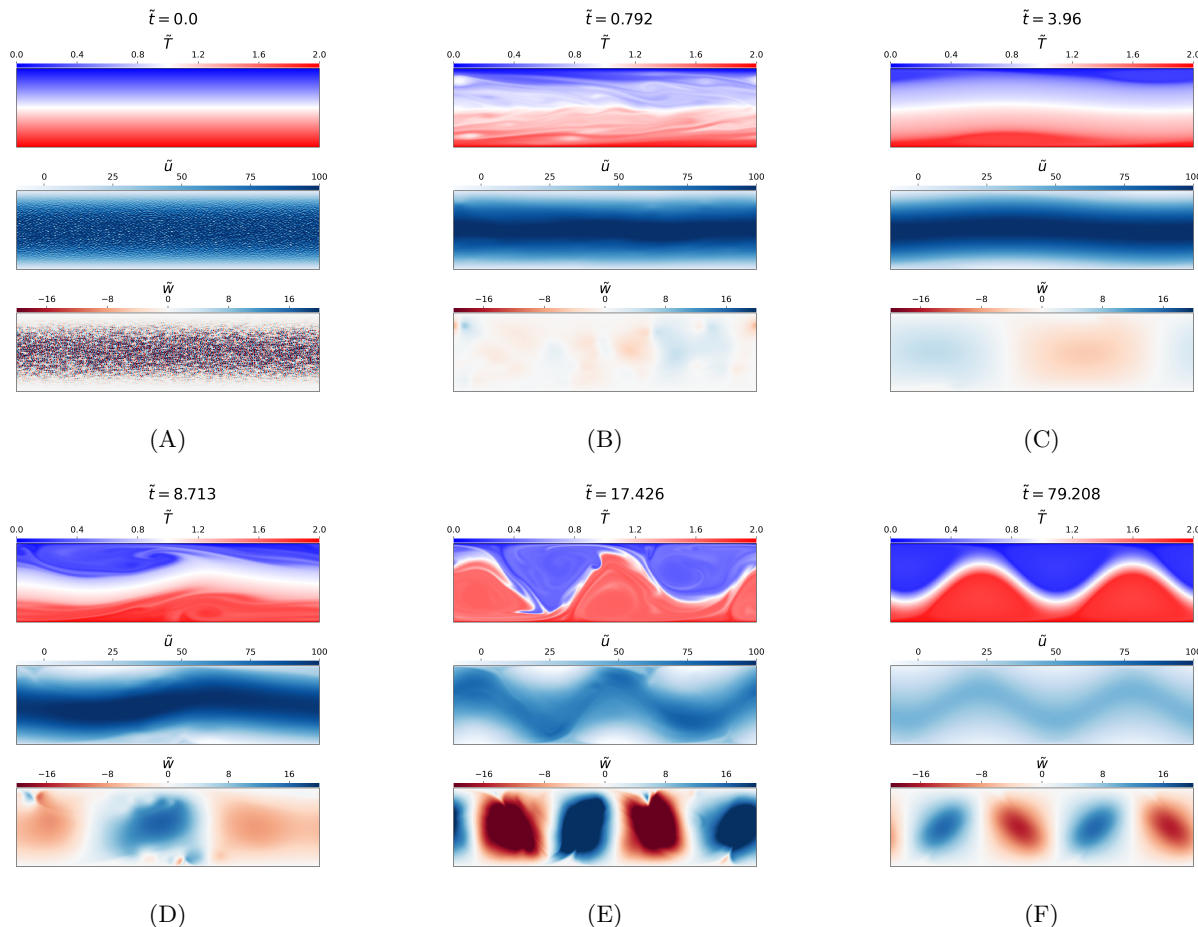


Figure 1.3: Simulation for $Re_\tau = 200$, dimensionless temperature \tilde{T} , dimensionless horizontal velocity \tilde{u} and dimensionless vertical velocity \tilde{w} for different dimensionless time \tilde{t} : (A) Initial state with white noise. (B) First transitory state. (C) Meta-stable state. (D) Second transitory state. (E) Stabilisation of the statistically steady state. (F) statistically steady state.

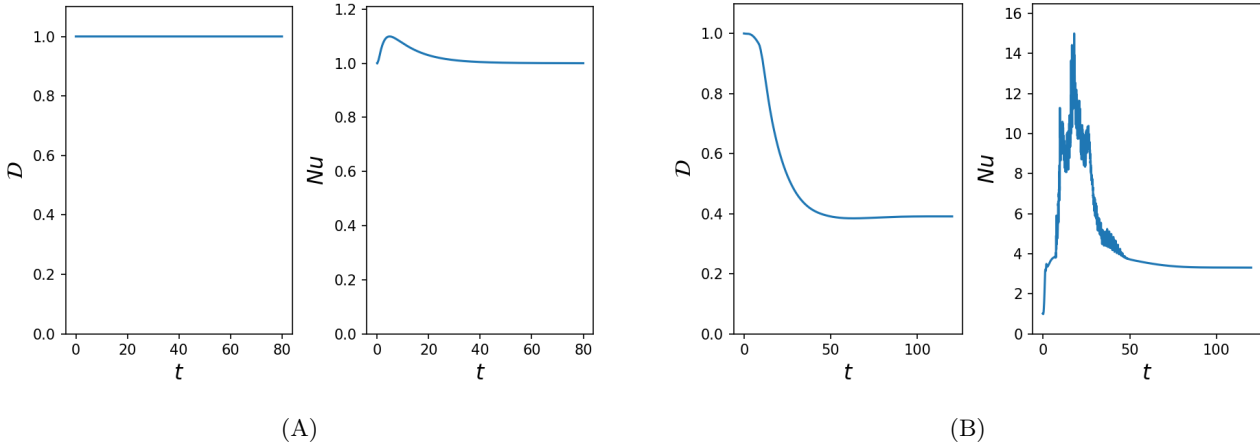


Figure 1.4: Flow rate $\mathcal{D}(t)$ and Nusselt $Nu(t)$ for different Re_τ : (A) $Re_\tau = 100$: steady state reached for $t \simeq 30$. (B) $Re_\tau = 200$: steady state reached for $t \simeq 60$.

We notice that for any Re_τ , we have a stationary or a statistically steady state which is reached (not shown here). Indeed, $\mathcal{D}(t)$ and $Nu(t)$, from a certain time t_p , do not vary anymore or oscillate around an average value no longer varying over time. For high Re_τ , the state still vary in time, but the pattern always repeats itself (not shown here). It is interesting to notice that the flow rate drop in the statistically steady state and that the heat flux at the wall increases. For example for $Re_\tau = 200$, the heat flux is multiplied by four. The drop in flow and the increase in the Nusselt are related to an increase in the vertical fluxes of horizontal momentum and heat, allowed by the nonlinear flow.

1.3 Bifurcation diagrams

In this section we use our diagnostics $\mathcal{D}(t)$ and $Nu(t)$ in order to sketch bifurcation diagrams $\overline{\mathcal{D}}(Re_\tau)$ and $\overline{Nu}(Re_\tau)$ of the Poiseuille flow separating the laminar base state from the nonlinear regime. According to Orszag (Orszag 1971 [14]), the transition from the stationary state to the statistically steady state occurs at the critical Reynolds centerline $Re_c = 5772.22$ with

$$Re_c = \frac{Re_\tau^2}{2} \quad (1.21)$$

So we are looking for a bifurcation at a $Re_\tau = 107, 44$. Our results can be found [FIGURE 1.5](#). Whether we look at $\mathcal{D}(Re_\tau)$ or at $Nu(Re_\tau)$, we find that for $Re_\tau < 140$, their values are constants. However, from $Re_\tau \simeq 140$, they both change, $\mathcal{D}(Re_\tau)$ drops and $Nu(Re_\tau)$ rises. It is interesting to note that the bifurcation is less clear in the case of Nusselt.

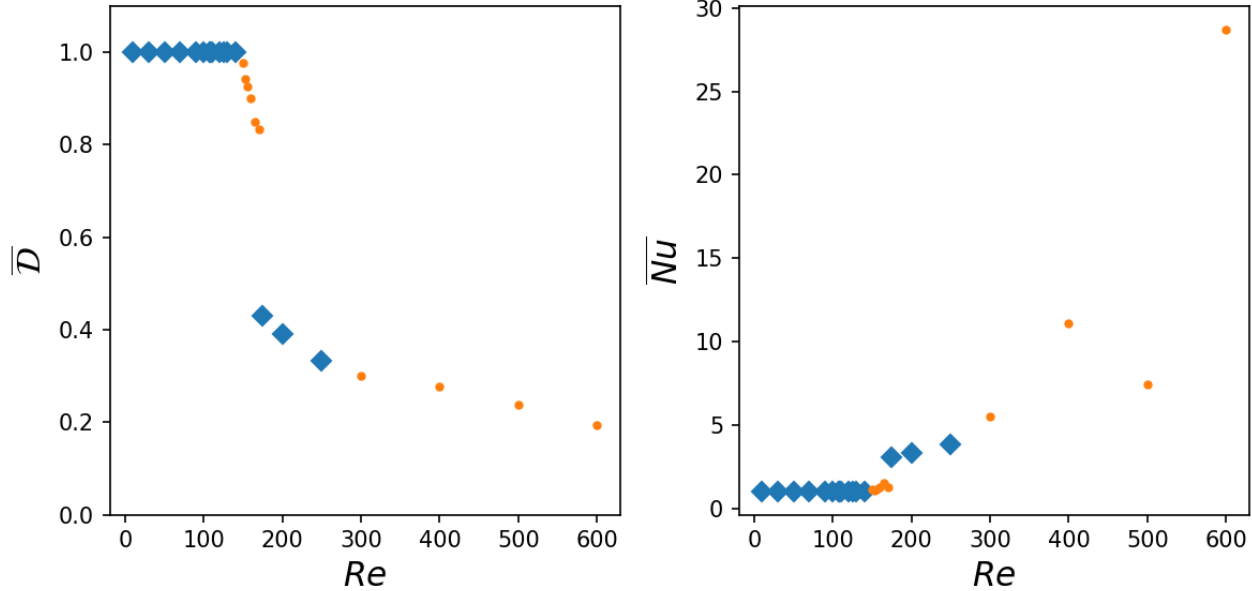


Figure 1.5: Bifurcation diagrams $\overline{D}(Re_\tau)$ on the left and $\overline{Nu}(Re_\tau)$ on the right. The temporal average is carried out only on the ten last friction time of the simulation in order to have the temporal average of the steady state. However, the simulation time may not be sufficient to reach the steady state. Thus, the variables are plotted in orange dots in the case where the steady state is not reached and in blue diamonds in the case where it is reached.

It seems that for us the bifurcation takes place around $Re_\tau \simeq 140$ and not around $Re_\tau \simeq 107$. A transition at 140 is not in agreement with the results of Orszag (Orszag 1971 [14]). This discrepancy may be explained by two ways. First, although we use a white noise, we cannot excite the most unstable mode, which determines the threshold, because the box is not equal to the wavelength of the critical mode or a multiple of this wavelength. The question would therefore be, how much must Re_τ be increased above the threshold, for the most unstable mode resolved by our box, to be effectively unstable. It would also be interesting to choose a box length corresponding to the wavelength of the critical mode or a multiple of this wavelength. Secondly, the problem may be due to the fact that we have the impression that the permanent state has been reached when it is not. The system may take more time to be destabilised. We could verify it by carrying out much longer simulations than what we have done, *ie* with friction times longer than 150. Due to lack of time, we decided instead to make progress on simulations of Poiseuille flow in non-planar channels.

2 Poiseuille flow dynamics in a channel with a wavy boundary

The objective of this second part is to understand some elements concerning the influence of a non-planar water-ice interface on its melting and on the flow. For this, we are going to use the Poiseuille flow used in [Part 1](#) to which we will add an asymmetry by changing the shape of the top wall. The problem has non-rectangular geometry, which cannot be handled by a spectral method that requires a Cartesian grid. To overcome it, we will implement a domain remapping method. For the boundary topography, we will always use a sinusoidal wave of wavelength as long as the box.

2.1 Model

Governing equations

Let us note $\delta(x, t)$ the position of the wavy boundary with respect to its mean value $z=h$ ([FIGURE 2.1A](#)). We take the system of the [Part 1](#) in which we just change the support of the flat top by a support whose shape varies according to x and t . The equations remain almost the same. Only the boundary conditions at $z=h$ change. They are replaced by

$$\underline{u}(z = h + \delta(x, t)) = 0, \quad T(z = h + \delta(x, t)) = T_t \quad (2.1\text{a-b})$$

which read in dimensionless form:

$$\tilde{\underline{u}}(\tilde{z} = 1 + \frac{\delta(x, t)}{h}) = 0, \quad \tilde{T}(\tilde{z} = 1 + \frac{\delta(x, t)}{h}) = \frac{T_t}{\Delta T}. \quad (2.2\text{a-b})$$

In order to have a system of equations that can be implemented in *Dedalus*, which requires a rectangular computational domain, we realise the following coordinates change:

$$\tilde{t}' = \tilde{t}, \quad \tilde{x}' = \tilde{x}, \quad \tilde{z}' = \frac{\tilde{z} + \frac{h_b}{h_t}}{1 + \frac{h_b}{h_t} + \frac{\delta}{h_t}} \quad (2.3\text{a-c})$$

We define, for improved readability in the derivation of the domain-remapped, the following variables

$$\gamma = \frac{h_b}{h_t}, \quad \beta = 1 + \gamma, \quad \delta(x, t) = \delta_f f(x, t), \quad \epsilon = \frac{\delta_f}{h_t}, \quad A(x, t) = \frac{1}{\beta + \epsilon f(x, t)} \quad (2.4\text{a-e})$$

with δ_f the topography amplitude and $f(x, t)$ the shape function, which is allowed to vary in time for reasons that will be explained later. We neglect the tildes for clarity from now on. By injecting the change of coordinates of [equations \(2.3\)](#) in [equations \(1.9\)](#) using [equations \(2.4\)](#), we obtain the following new equations

$$\partial_{x'} u - (\epsilon A z' \partial_x f) \partial_{z'} u + A \partial_{z'} w = 0 \quad (2.5\text{a})$$

$$\begin{aligned} \partial_{t'} \underline{u} - (\epsilon A z' \partial_t f) \partial_{z'} \underline{u} + u [\partial_{x'} \underline{u} - (\epsilon A z' \partial_x f) \partial_{z'} \underline{u}] + w A \partial_{z'} \underline{u} &= [-\partial_{x'} P + (\epsilon A z' \partial_x f) \partial_{z'} P] \underline{e}_x - A \partial_{z'} P \underline{e}_z - \frac{R i_\tau}{2} T \underline{e}_z \\ &+ \frac{1}{Re} [\partial_{x'^2} \underline{u} + A \epsilon z' (2\epsilon A \{\partial_x f\}^2 - \partial_{x^2} f) \partial_{z'} \underline{u} - (2\epsilon A z' \partial_x f) \partial_{z'} \partial_{x'} \underline{u} + (\{\epsilon A z' \partial_x f\}^2 + A^2) \partial_{z'^2} \underline{u}] + \underline{e}_x \end{aligned} \quad (2.5\text{b})$$

$$\begin{aligned} \partial_{t'} T - (\epsilon A z' \partial_t f) \partial_{z'} T + u [\partial_{x'} T - (\epsilon A z' \partial_x f) \partial_{z'} T] + w A \partial_{z'} T &= \\ + \frac{1}{Re P_r} [\partial_{x'^2} T + A \epsilon z' (2\epsilon A \{\partial_x f\}^2 - \partial_{x^2} f) \partial_{z'} T - (2\epsilon A z' \partial_x f) \partial_{z'} \partial_{x'} T + (\{\epsilon A z' \partial_x f\}^2 + A^2) \partial_{z'^2} T] \end{aligned} \quad (2.5\text{c})$$

$$\underline{u}(z' = 0) = 0 \quad (2.5d)$$

$$\underline{u}(z' = 1) = 0 \quad (2.5e)$$

$$T(z' = 0) = \frac{T_b}{\Delta T} \quad (2.5f)$$

$$T(z' = 1) = \frac{T_t}{\Delta T}. \quad (2.5g)$$

We do not inject [equations \(2.5\)](#) in this form in *Dedalus*, the modified system is detailed and explained in [APPENDIX A.3](#). [FIGURE 2.1B](#) represents schematically the shape of the system after the domain remapping. We can see that the boundary conditions are easier, the system is now just a rectangle, just like a plane Poiseuille flow. However as a consequence the equations get many geometrically-induced additional terms.

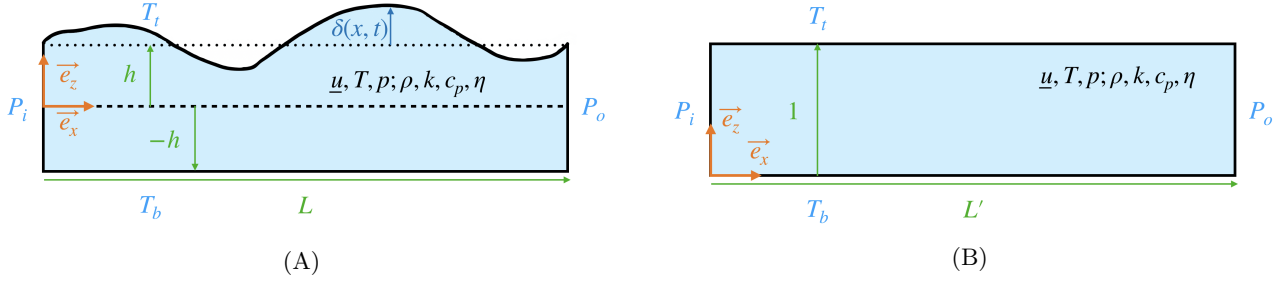


[Figure 2.1: Schematic of the system : \(A\) Wavy system without domain remapping. \(B\) Wavy system with domain remapping.](#)

In this paper, we will limit ourselves to a sinusoidal topography of the form

$$f(x, t) = \sin(k_x x) \tanh(r_0 t) \quad (2.6)$$

with $k_x = \frac{2\pi}{\lambda}$, λ being the wavelength of the sinusoidal topography and r_0 a parameter allowing to vary the speed of the topography growth. The hyperbolic tangent part allows us to keep the initial conditions used in the [Part 1](#). Note that starting from a flat boundary is especially useful because there isn't a simple exact analytical laminar base state solution for a wavy boundary.

Variables of interest

We keep the variables of interest of the [Part 1](#) in order to identify if we reach a steady state. However we change their application from h to $h + \delta(x, t)$. In addition to those, we consider the heat-flux pattern $q_w(x, t)$ of the flow at the top wall, *i.e.*:

$$q_w(x, t) = -k \partial_z T(z = h + \delta(x, t)). \quad (2.7)$$

Applying it to the stationary state of [equation \(1.4c\)](#), we get

$$q_{w_p} = -\frac{k \Delta T}{2h}. \quad (2.8)$$

We will use q_{w_p} as a normalisation factor to define our **fifth variable of interest** $\mathcal{Q}_w(x, t)$, the heat flux at the top wall scaled by q_{w_p} :

$$\mathcal{Q}_w(x, t) = \frac{q_w}{q_{w_p}}. \quad (2.9)$$

We use $\mathcal{Q}_w(x, t)$ to define our **sixth variable of interest** $\overline{\mathcal{Q}_w}(x)$ corresponding to its averaged according to t :

$$\overline{\mathcal{Q}_w}(x) = \langle \mathcal{Q}_w(x, t) \rangle_t . \quad (2.10)$$

Note that we perform the average once the permanent state has been reached, in order to have the average heat flux of the steady state. Indeed, we would like to know the long-term (time-averaged) effect of the wavy boundary on the heat flux pattern. This will help us to understand how the topography will vary by knowing where the melting will be the strongest.

Our perturbation being sinusoidal, we can associate a particular wave vector to it, it is the number k_x defined before as $k_x = \frac{2\pi}{\lambda}$, λ being the wavelength of the sinusoidal topography. We may expect the heat flux pattern at the top of the wall to depend linearly on the topography amplitude for small amplitudes (even though the hydrodynamic equations are nonlinear) and non-linearly for large amplitudes since the system depends non-linearly on the topography. We will not only have the mode k_x in response but also other modes. In order to understand the impact of all modes, we carry out a Fourier transformation of the heat flux. This Fourier transform being discrete due to the fact that we have a discretization of the x space, we can write it :

$$TF(\overline{\mathcal{Q}_w}) = \sum_n A_n(\overline{\mathcal{Q}_w}) \exp(ik_n x + \Phi_n(\overline{\mathcal{Q}_w})) \quad (2.11)$$

with $k_n = nk_x$ the wave vector norm, $A_n(\overline{\mathcal{Q}_w})$ the module and $\Phi_n(\overline{\mathcal{Q}_w})$ the phase of the n-th Fourier coefficient. We study in particular the first two modes 0 and 1, the mode 0 corresponding to the average value of $\mathcal{Q}_w(x)$ according to x and the mode 1 the linear response of the system. It is important to note that for small perturbations, the mode 1 normally controls the morphological stability whereas for stronger perturbations, the other harmonic starts to have an important role too. These two particular modes will give us our **seventh variable of interest** $A_0(\overline{\mathcal{Q}_w})$, our **eighth variable of interest** $A_1(\overline{\mathcal{Q}_w})$ and our **ninth variable of interest** $\Phi(\overline{\mathcal{Q}_w}) = \Phi_1(\overline{\mathcal{Q}_w}) - \Phi_{topo}$, where Φ_{topo} is the phase of the topography. $A_0(\overline{\mathcal{Q}_w})$ allows us to identify the global impact of the interface on the heat flux. $A_1(\overline{\mathcal{Q}_w})$ allows us to identify the strength of the linear response of the heat flux to the interface perturbation. $\Phi(\overline{\mathcal{Q}_w})$ allows us to identify the phase difference between the heat flux perturbation and the topography. If $\Phi \in [-\frac{\pi}{2}, \frac{\pi}{2}][2\pi]$, it corresponds to a phase lag which tends to increase the topography. Whereas, if $\Phi \in [\frac{\pi}{2}, \frac{3\pi}{2}][2\pi]$, it corresponds to a phase lag which tends to smooth the topography.

We also consider similarly-defined hydrodynamic diagnostics based on the shear stress, which are of interest in flow-granular-media interaction studies. The shear at the top wall $\tau_w(x, t)$ being defined by

$$\tau_w(x, t) = \eta \partial_z u(z = h_t + \delta(x, t)). \quad (2.12)$$

Therefore by applying the same logic we have

$$\mathcal{T}_w(x, t) = \frac{\tau_w}{\tau_{w_p}} \quad (2.13)$$

$$\overline{\mathcal{T}_w}(x) = \langle \mathcal{T}_w(x, t) \rangle_t \quad (2.14)$$

$$TF(\overline{\mathcal{T}_w}) = \sum_n A_n(\overline{\mathcal{T}_w}) \exp(ik_n x + \Phi_n(\overline{\mathcal{T}_w})). \quad (2.15)$$

Defining the variables $A_0(\overline{\mathcal{T}_w})$, $A_1(\overline{\mathcal{T}_w})$ and $\Phi(\overline{\mathcal{T}_w}) = \Phi_1(\overline{\mathcal{T}_w}) - \Phi_{topo}$. It is important to note that in the case of granular medium, the source of instability is not the same as for water-ice system. According to Charru (Charru 2013 [4]), in granular medium, instability results from the destabilising action of fluid inertia, which induces a phase advance of the shear stress relative to the bed disturbance. Thus, the important point is to look if Φ is slightly larger than π .

The heat flux and the shear normal to the wall are interesting diagnostics since they are part of the global momentum and energy budget of the system taking into account the topography. The flow and the shear are chosen vertical here for simplicity. Note also that the vertical flux gives information on the local vertical motion of the wall by phase change.

2.2 Influence of topography

The goal of this study is to understand some effects of the interaction between the topography and the flow. In particular, we want to understand how the heat flux and shear at the top wall is modified by the topography.

Simulation parameters

We fix $Re_\tau = 100$ and we vary the parameter ϵ from 0.01 to 0.4 (ϵ tested : 0.01, 0.05, 0, 10, 0.15, 0.20, 0.25, 0.30, 0.35, 0.4). In particular, we will focus our attention on the results for two extremes values, a small topography of $\epsilon = 0.05$ and a stronger one of $\epsilon = 0.4$. We use the *RK222* timestepper, a safety parameter of the CFL of 0.05, a spatial resolution $N_x = 512$ in the e_x direction with the *RealFourier* discretization method of *Dedalus* and in the e_z direction, we choose a resolution $N_z = N_x/2 = 256$ with the *ChebyshevT* discretization method of *Dedalus*.

Overall results

For almost all ϵ we have reached a stationary state or a statistical steady state by running our simulations on a friction time between 60 and 120. There is just for $\epsilon = 0.35$ that we could not reach one. It would have been necessary for this ϵ to run the simulation longer. However, due to lack of time, we chose not to study it.

As in [Part 1](#), we observe two different final regimes. The first is a laminar stationary state, which no longer vary in time. It is observed for $\epsilon < 0.1$. We can see the shape of this flow in [FIGURES 2.2A](#) and [2.2B](#), where the dimensionless temperature T and the dimensionless horizontal velocity u are respectively represented for $\epsilon = 0.05$ at a friction time $t = 63$. The flow is very close to that of [Part 1](#) for low Reynolds, such as $Re_\tau = 100$ with plane walls ([FIGURES 1.2C](#)). The second final state is a statistically steady state, varying over time around an average value. It is observed for $\epsilon \geq 0.1$. We can see the shape of this flow in [FIGURES 2.3A](#) and [2.3B](#) where the temperature and the velocity for $\epsilon = 0.40$, at a friction time $t = 75$. We observe re-circulation cells at the maximum and minimum of the topography. Moreover, looking at the flow over time, these cells are advected and then recreated indefinitely (not shown here).

In order to study the evolution of the topography, it is interesting to study the wall heat flux and the wall shear. In the case of a water-ice system, it is the heat flux at the wall that will mainly guide the evolution of the interface. This quantity is the most interesting in the case of our study. In the case of a fluid-granular medium system, it is rather the shear at the wall that will guide the evolution of the interface. This quantity is not the most relevant in the case of our study. However, it is important to study it for its application to granular media. In order to carry out this study, as described in the [Subsection 2.1](#), we carry out the Fourier transformation of these quantities. This allows us to plot the graph of the Fourier transformation modulus A_n as a function of $n = \frac{k_n}{k_x}$. In the case of $\epsilon < 0.1$, we notice, that only two coefficients are important, for both the heat flux and the shear. They are the mode 0 and the mode 1 ([FIGURES 2.2C](#), [2.2D](#)). On the contrary, for $\epsilon \geq 0.1$, higher harmonics appear. We even notice, for the case of wall shear, that mode 0 is no longer preponderant, mode 1 starts dominating instead ([FIGURES 2.3C](#), [2.3D](#)). These results are explained by the fact that for small disturbances, the response of the system is mainly linear, so there is only mode 0 and mode 1. On the other hand, for higher disturbances, the non-linearities drive the flow, revealing higher harmonics ($n \geq 2$).

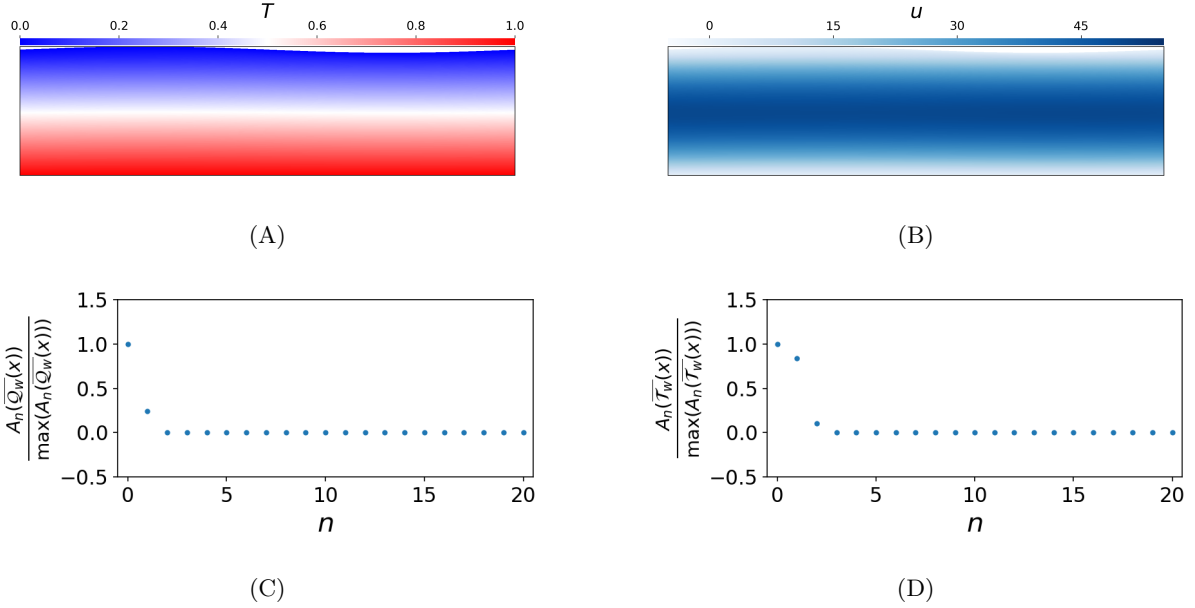


Figure 2.2: *Simulation for $Re = 100$ and $\epsilon = 0.05$.* (A) *Snapshot of the dimensionless temperature T at $t = 63$ (steady state reached).* (B) *Dimensionless horizontal speed u at $t = 63$ (steady state reached).* (C) $A_n(\overline{Q_w})$, module of the mean over time of Fourier coefficients of equation (2.11). (D) $A_n(\overline{T_w})$, module of the mean over time of Fourier coefficients of equation (2.15). The error bars correspond to the standard deviation calculated on the permanent state. They are smaller than the marker size, hence not visible since the flow is laminar.

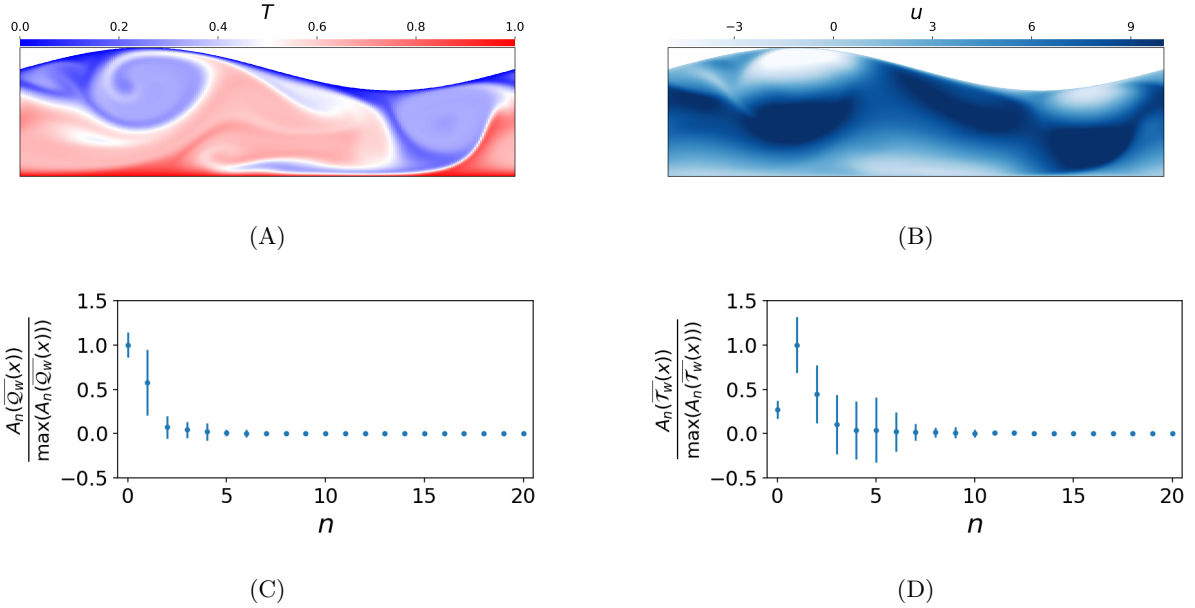


Figure 2.3: *Simulation for $Re_\tau = 100$ and $\epsilon = 0.4$.* (A) *Snapshot of the dimensionless temperature T at $t = 75$ (steady state reached).* (B) *Dimensionless horizontal speed u at $t = 75$ (steady state reached).* (C) $A_n(\overline{Q_w})$, module of the mean over time of Fourier coefficients of equation (2.11). (D) $A_n(\overline{T_w})$, module of the mean over time of Fourier coefficients of equation (2.15). The error bars correspond to the standard deviation calculated on the permanent state.

We are now particularly interested in A_0 , A_1 and Φ as functions of ϵ . The results are plotted in FIGURES 2.4 for heat flux. We have filled in red the areas where $\Phi \in [-\frac{\pi}{2}, \frac{\pi}{2}][2\pi]$; they correspond to a phase lag which tends to increase the topography in the case of water-ice system. We have filled in green the areas where

$\Phi \in [\frac{\pi}{2}, \frac{3\pi}{2}][2\pi]$; they correspond to a phase lag which tends to smooth the topography in the case of water-ice system. We do the same for the shear [FIGURES 2.6](#). Note that for the shear, those areas are not as relevant as for the heat flux. In the case of water-ice system, it is not clear if the wall shear will boost phase change. The phase is more interesting for granular medium. The horizontal distribution of heat flux and shear is shown more qualitatively on the [FIGURES 2.5](#) and [2.7](#) for $\epsilon = 0.5$ and for $\epsilon = 0.4$.

Heat flux results

In the case of heat flux, A_0 and A_1 ([FIGURES 2.4A](#) and [2.4B](#)) seem to have a linear behaviour up to $\epsilon = 0.25$; above it seems that the behaviour is more difficult, it even seems to decrease. Concerning the phase ([FIGURE 2.4C](#)), we see that on average for $\epsilon < 0.1$, the heat flow is in phase opposition with the topography, which means that the interface is morphologically stable (green shading). Above, on the contrary, it is in phase. The horizontal profiles of the heat flux and shear at the wavy boundary are shown in [FIGURES 2.5](#). For $\epsilon = 0.05$, the total heat flux seems to be the superposition of the mode 0 and the mode 1. The maximum of the heat flux is in the green area which means that it is in opposition with the topography. On the contrary for $\epsilon = 0.4$, the total heat flux seems not to be the superposition of the mode 0 and the mode 1. The maximum of the heat flux is in the red area which means that it in phase with the topography.

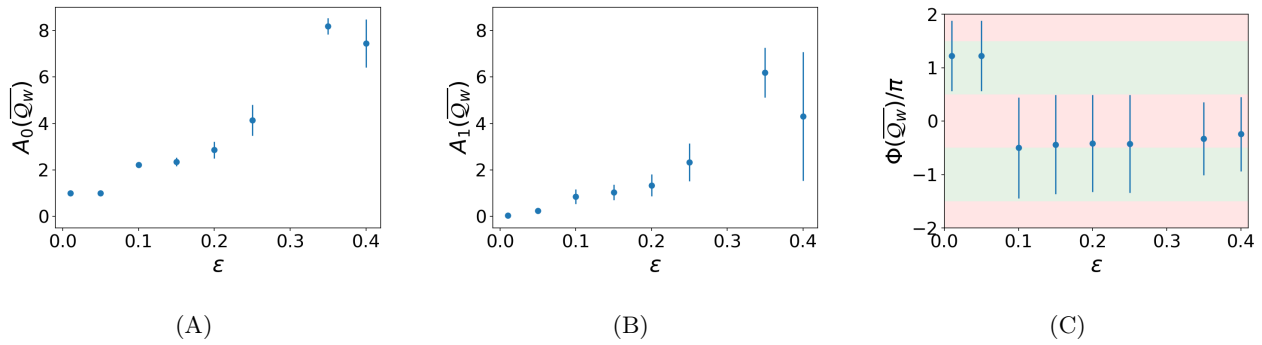


Figure 2.4: *Simulation for $Re_\tau = 100$, Fourier coefficients from equation (2.11) in terms of ϵ the topography amplitude. The error bars correspond to the standard deviation calculated on the permanent state.* (A) $A_0(\overline{Q_w})(\epsilon)$, module of mode 0. (B) $A_1(\overline{Q_w})(\epsilon)$, module of mode 1. (C) $\Phi(\overline{Q_w})(\epsilon)$, phase lag with respect to topography. The areas where $\Phi \in [-\frac{\pi}{2}, \frac{\pi}{2}][2\pi]$ are represented in red. They correspond to the increase of the topography. The areas where $\Phi \in [\frac{\pi}{2}, \frac{3\pi}{2}][2\pi]$ are represented in green. They correspond to the smoothing of the topography.

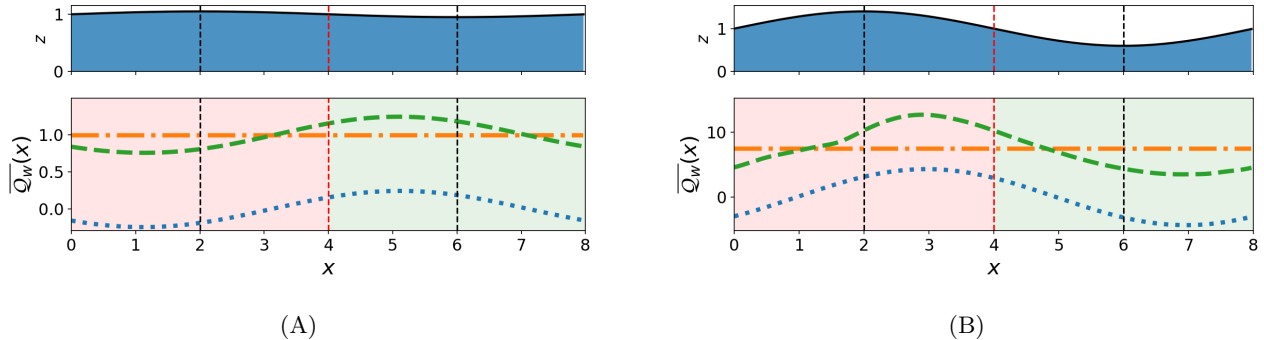


Figure 2.5: Heat flux as a function of x for $Re_\tau = 100$ at two different ϵ . On the bottom graph, green thick dashes represent all modes of $\overline{Q}_w(x)$, thick orange dash-dots represent the mode 0 of $\overline{Q}_w(x)$ and thick blue dots represent the mode 1 of $\overline{Q}_w(x)$. The area where $x \in [0, 4]$ is shaded in red. If $\max(\overline{Q}_w(x))$ is in this area, it will be in favour of the increase of the topography. The area where $x \in [4, 8]$ is shaded in green. If $\max(\overline{Q}_w(x))$ is in this area, it will be in favour of the smoothing of the topography. On the top graph we represent the flow, between $z = 0$ and $z = 1 + \epsilon f$; black line represents the topography. On both graphs, the black dashed lines show the max and the min of the topography and the horizontal red dashes show the limit between the green and red area: (A) Results for $\epsilon = 0.05$. (B) Results for $\epsilon = 0.4$.

The linear behaviour of A_0 and A_1 can be partly explained by the fact that the larger the disturbance, the greater the response of the system. The decrease at higher ϵ can be explained by the fact that the harmonics take over. The fact that values of A_0 and A_1 are greater than 1, in FIGURES 2.4A and 2.4B, shows that with the addition of the topography, the melting will be greater than for a flow with a plane wall. For the phase, as it is in phase opposition with the flow for $\epsilon < 0.1$, we will have on average a smoothing of the topography. On the contrary for $\epsilon \geq 0.1$, the fact that we are in phase with the topography will tend to make the topography grow. Although we are in phase, we are not exactly there, so in addition to increasing, the topology will also tend to drift.

Note that in this case, Φ is not equal to zero. Thus,

Wall shear results

In the case of shear, A_0 and A_1 (FIGURES 2.6A and 2.6B) have a different behaviour. A_0 seems to only decrease starting from 1 for small ϵ and reaching almost 0 for larger ϵ . On the contrary A_1 does not seem to have any particular behaviour, its value only seems to vary around 1. Concerning the phase (FIGURE 2.6C), Φ is always slightly larger than π , which means that the vertical shear is always maximum (minimum) just downstream of the topography minimum (maximum). We can see these results visually on the FIGURES 2.7. For $\epsilon = 0.05$, the total shear seems to be the superposition of the mode 0 and the mode 1. What is more, the maximum of the heat flux is in the green area which means that it is in opposition with the topography. On the contrary for $\epsilon = 0.4$, the total shear seems not to be the superposition of the mode 0 and the mode 1. As for $\epsilon = 0.05$, the maximum of the shear is in the green.

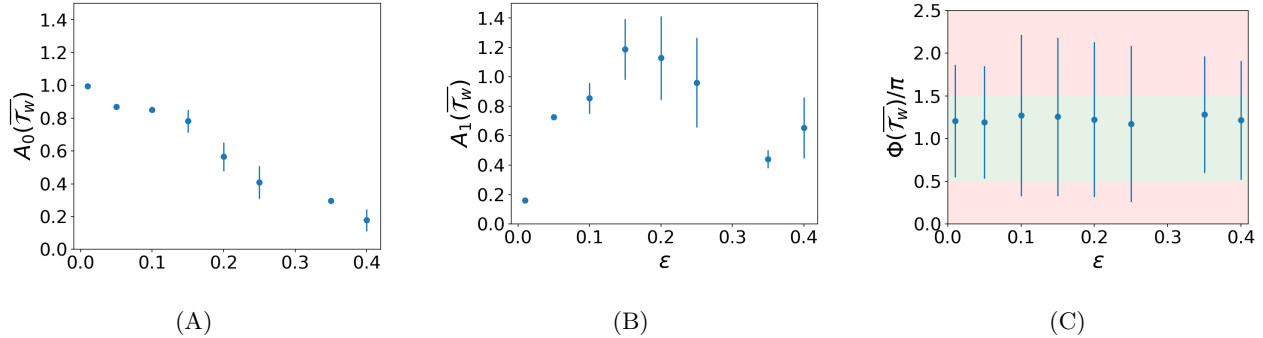


Figure 2.6: Simulation for $Re_\tau = 100$, Fourier coefficients from equation (2.15) in terms of ϵ the topography amplitude. The error bars correspond to the standard deviation calculated on the permanent state. (A) $A_0(\bar{T}_w)(\epsilon)$, module of mode 0. (B) $A_1(\bar{T}_w)(\epsilon)$, module of mode 1. (C) $\Phi(\bar{T}_w)(\epsilon)$, phase lag with respect to topography. The areas where $\Phi \in [-\frac{\pi}{2}, \frac{\pi}{2}][2\pi]$ are represented in red. The areas where $\Phi \in [\frac{\pi}{2}, \frac{3\pi}{2}][2\pi]$ are represented in green.

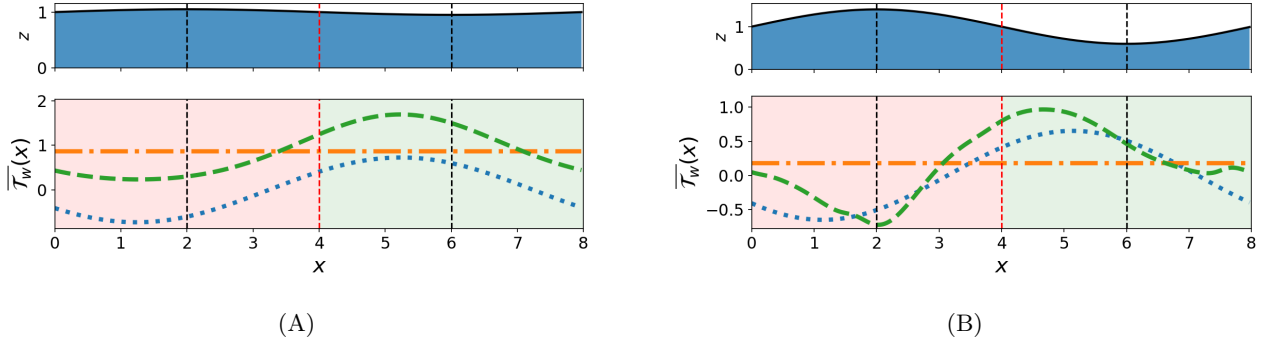


Figure 2.7: Wall shear as a function of x for $Re_\tau = 100$ at two different ϵ . On the bottom graph, green thick dashes represent all modes of $\bar{T}_w(x)$, thick orange dash-dots represent the mode 0 of $\bar{T}_w(x)$ and thick blue dots represent the mode 1 of $\bar{T}_w(x)$. The area where $x \in [0, 4]$ is shaded in red. The area where $x \in [4, 8]$ is shaded in green. On the top graph we represent the flow, between $z = 0$ and $z = 1 + \epsilon f$; black line represents the topography. On both graphs, the black dashed lines show the max and the min of the topography and the horizontal red dashes show the limit between the green and red area: (A) Results for $\epsilon = 0.05$. (B) Results for $\epsilon = 0.4$.

For the shear, when the amplitude of the topography increases, we would expect the coefficients A_n to also increase. Indeed, we have noticed that the more the amplitude the topography was important, the more the average flow decreased (not shown here). This fact means that the opposition force of the walls against the flow increases and, as a consequence, the shear. However, here we only look at the shear which does not composed the all opposition for. Indeed, the pressure also comes into account in the opposition force against the flow because the walls are no longer flat. It is also important to note that the calculated shear is not the one tangential to the wall but the one tangential to e_z . It would be physically more relevant to study the tangential shear instead, because it corresponds better to the opposition force. Moreover, in reality, if we really wanted to study the opposition force, we would have to start from the tensor of the constraints. It would then be shown that the shear is not sufficient for the study of the opposition force. It would therefore be more relevant for more in-depth studies to change the parameters of the simulation accordingly. Concerning the phase, Φ is always slightly larger than π . Thus, it seems that our results are in the conditions to create instability in granular medium. Charru (Charru 2013 [4]) explains that the shear will tear off more grains where it is maximum, just before the hump of the granular bed. The grains will be deposited on the ridge. This process therefore tends to increase the amplitude of the crest.

Conclusion

The domain remapping technique has been implemented in *Dedalus* to allow spectral simulations of a Poiseuille flow in a physical non-rectangular domain. Results for a Poiseuille flow in a rectangular channel were first discussed and used as a starting point for simulations in channels with a wavy boundary. We find that the Poiseuille laminar base state is stable for low shear Reynolds number and unstable for high with a bifurcation around $Re_\tau \simeq 140$. Interestingly, at moderately-large Reynolds number, intermediate meta-stable states arise, which transition to the final nonlinear statistical steady state over long time scales. For wavy channels, we focused on $Re_\tau = 100$. We found that wavy topography tends to increase the wall heat flux, which could lead to a faster ice melting than a plane topography. For low topography amplitude (less than 10% of box height), the heat flux tends to be on average in opposition with the topography pattern, which could lead to the smoothing of the surface. However, for larger topography amplitude (more than 10% of box height), the heat flux tends to be on average in phase with the topography, which could lead to the increase of the topography pattern. Moreover in this case, the phase is slightly in advance, which could induce a drift of the pattern. As a consequence, morphological instabilities are possible at a water-ice interface; at least for $Re_\tau = 100$ and high enough topography amplitude (more than 10% of box height) in 2D. It would be interesting to look at higher Reynolds in order to see if morphological instabilities could happen with smaller topography amplitude. For the granular medium, future studies should implement a wall shear calculated from the constraint tensor rather than a simple derivation along vertical coordinate. It would be more relevant for an application to real systems to switch to 3D. The calculations of the domain remapping in 3D have been carried out and show that its implementation is possible (not written in this report). However, it will be necessary to take into account that the computation cost will be more important than in 2D.

Bibliography

- [1] P. N. Blumberg and R. L. Curl. Experimental and theoretical studies of dissolution roughness. *Journal of Fluid Mechanics*, 65:735–751, 1974.
- [2] M. Bushuk, D. M. Holland, T. P. Stanton, A. Stern, and C. Gray. Ice scallops: a laboratory investigation of the ice–water interface. *Journal of fluid mechanics*, 873:942–976, 2019.
- [3] K. L. Carey. Observed configuration and computed roughness of the underside of river ice, st. croix river, wisconsin. *Geological Survey Professional Paper*, 550:B192–B198, 1966.
- [4] F. Charru, B. Andreotti, and P. Claudin. Sand ripples and dunes. *Annual Review of Fluid Mechanics*, 45:469–493, 2013.
- [5] L.-A. Couston, E. Hester, B. Favier, J. R. Taylor, P. R. Holland, and A. Jenkins. Topography generation by melting and freezing in a turbulent shear flow. *Journal of Fluid Mechanics*, 911:1–29, 2021.
- [6] R. L. Curl. Scallops and flutes. cave research group great britain. *Trans*, 7:121, 1966.
- [7] G. Falkovich and N. Vladimirova. Turbulence appearance and nonappearance in thin fluid layers. *Physical review letters*, 121:164501, 2018.
- [8] R. R. Gilpin, T. Hirata, and K. C. Cheng. Wave formation and heat transfer at an ice-water interface in the presence of a turbulent flow. *Journal of Fluid Mechanics*, 99:619–640, 1980.
- [9] T. J. Hanratty. Stability of surfaces that are dissolving or being formed by convective diffusion. *Annual Review of Fluid Mechanics*, 13:231–252, 1981.
- [10] B. W. Hobson, A. D. Sherman, and P. R. McGill. Imaging and sampling beneath free-drifting icebergs with a remotely operated vehicle. *Deep Sea Research Part II: Topical Studies in Oceanography*, 58:1311–1317, 2011.
- [11] J. Jiménez. Transition to turbulence in two-dimensional poiseuille flow. *Journal of Fluid Mechanics*, 218:265–297, 1990.
- [12] M. C. Kennicutt, D. Bromwich, D. Liggett, B. Njåstad, L. Peck, S. R. Rintoul, C. Ritz, M. J. Siegert, A. Aitken, C. M. Brooks, et al. Sustained antarctic research: a 21st century imperative. *One Earth*, 1:95–113, 2019.
- [13] J. M. Nelson, S. R. McLean, and S. R. Wolfe. Mean flow and turbulence fields over two-dimensional bed forms. *Water Resources Research*, 29:3935–3953, 1993.
- [14] S. A. Orszag. Accurate solution of the orr–sommerfeld stability equation. *Journal of Fluid Mechanics*, 50:689–703, 1971.
- [15] H. D. Pritchard, S. R. M. Ligtenberg, H. A. Fricker, D. G. Vaughan, M. R. van den Broeke, and L. Padman. Antarctic ice-sheet loss driven by basal melting of ice shelves. *Nature*, 484:502–505, 2012.
- [16] E. Rignot, S. Jacobs, J. Mouginot, and B. Scheuchl. Ice-shelf melting around antarctica. *Science*, 341:266–270, 2013.
- [17] D. Sutherland, R. H. Jackson, C. Kienholz, J. M. Amundson, W. Dryer, D. Duncan, E. Eidam, R. Motyka, and J. Nash. Direct observations of submarine melt and subsurface geometry at a tidewater glacier. *Science*, 365:369–374, 2019.
- [18] R. M. Thomas. Size of scallops and ripples formed by flowing water. *Nature*, 277:281–283, 1979.
- [19] M. S. D. Wykes, J. Mac Huang, G. A. Hajjar, and L. Ristroph. Self-sculpting of a dissolvable body due to gravitational convection. *Physical Review Fluids*, 3:043801, 2018.
- [20] R. K. Zeytounian. Modélisation asymptotique en mécanique des fluides newtoniens. *Springer Science & Business Media*, 15:152, 1994.
- [21] F. Zonta and A. Soldati. Stably stratified wall-bounded turbulence. *Applied Mechanics Reviews*, 70:17, 2018.

A Appendix

A.1 Zero-divergence white noise

In order to create a zero-divergence white noise on the speed, we use an intermediate function g . g is a white noise field generated in *Python* on which we have applied a sinusoidal envelope so that it is zero at the boundaries and maximum at the centre of the flow, such as the speed of the stationary Poiseuille plan solution. From g , we define a zero-divergence white noise speed $\underline{u}_0 = (u_0, w_0)$ as :

$$u_0 = -\partial_z g \quad (\text{A.1})$$

$$w_0 = \partial_x g \quad (\text{A.2})$$

A.2 Resolution parameters

During the first simulations, we have had several ringing issues. Ringing is a phenomenon that can appear during a numerical simulation. It corresponds to numerical instabilities which appear spontaneously during a simulation causing chaotic parasitic behaviours. We then have non-physical results that can cause the divergence of the simulation [11]. The [FIGURE A.1](#) is an example. At the beginning, it looks like the simulation run well ([FIGURE A.1A](#)), but quickly ringing appears on the centre of the dimensionless temperature \tilde{T} and the dimensionless horizontal velocity \tilde{u} ([FIGURE A.1B](#)), as we can see with the chaotic parasitic behaviours. From there, the system gets carried away and diverges ([FIGURE A.1C](#)).

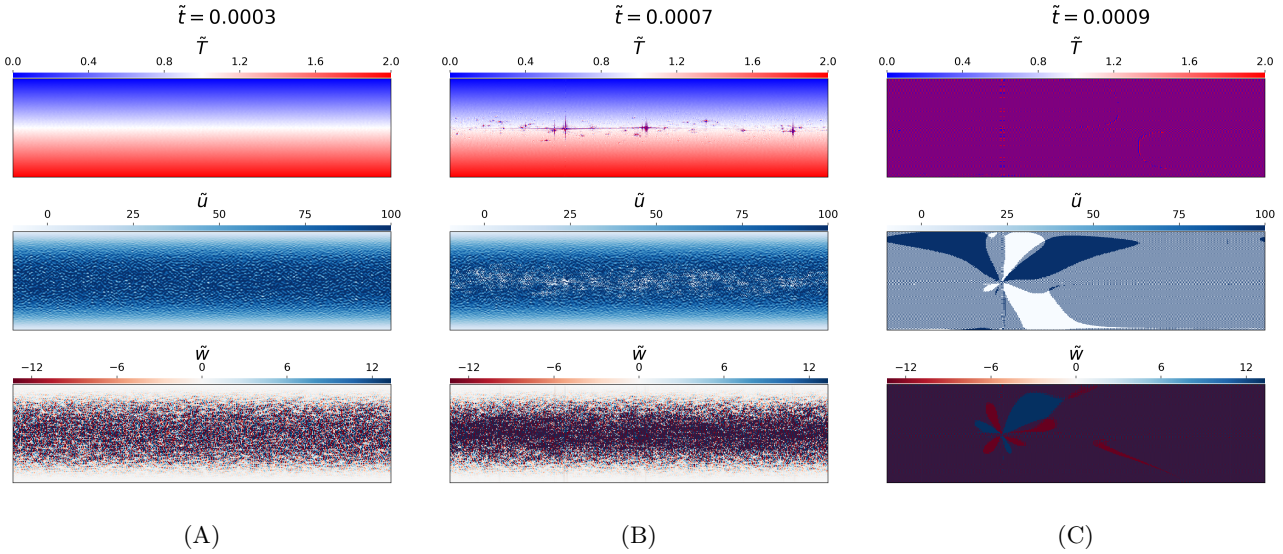


[Figure A.1](#): *Simulation for $Re = 200$, dimensionless temperature \tilde{T} , dimensionless horizontal velocity \tilde{u} and dimensionless vertical velocity \tilde{w} for different dimensionless time \tilde{t} :* (A) *The simulation starts to run, there is no ringing.* (B) *The ringing starts to appear.* (C) *The simulation has completely diverged.*

To avoid this type of phenomenon, several resolution parameters can be changed. In our case, we studied the influence of the timestepper, the safety parameter of the CFL and the spatial resolution by performing a sweep of these three parameters. The timestepper is the algorithm used to time integrate the solution forward. The safety parameter is a prefactor multiplying the time step calculated via the CFL condition, which is typically smaller than one thus reducing the time step and stabilising time integration. Finally, the spatial resolution corresponds to the number of points that we take spatially to solve our problem. In the e_x direction, we have a resolution noted N_x in the *RealFourier* discretization method of *Dedalus* and in the e_z direction, a resolution $N_z = N_x/2$ in the *ChebyshevT* discretization method of *Dedalus*.

The timesteppers tested are called *RK222*, *SBDF1* and *SBDF2*, we varied the safety parameter of the CFL from 0.01 to 1 and we tested three spatial resolutions $N_x = \{256, 512, 1024\}$. For example on the [FIGURE A.1](#),

we have the *RK222* timestepper, a safety parameter of the CFL of 1 and a spatial resolution $N_x = 512$. It comes out of this study that for our system of [Part 1](#), the most efficient timestepper is the *RK222* and the safety parameter of the CFL should be less than 0.1. With this timestepper and this safety parameter of the CFL, a spatial resolution of 1024 is not required. It is then necessary to use either 256 or 512, depending on the case.

We therefore made the choice to settle with the following parameters: the *RK222* timestepper, a safety parameter of the CFL of 0.1 and a spatial resolution $N_x = 512$.

A.3 Domain Remapping Optimisation

Rather than injecting the equations [equations \(2.5\)](#) directly in this form into *Dedalus*, ... proposes adding optimisation terms C_1, C_2, C_3, C_4 in order to facilitate numerical calculations, by rewriting the [equations \(2.5a\)](#), [\(2.5b\)](#) and [\(2.5c\)](#) as follows :

$$C_1 \nabla' \underline{u} = C_1 \nabla' \underline{u} + AddMC$$

avec $AddMC = \partial_{x'} u - (\epsilon A z' \partial_x f) \partial_{z'} u + A \partial_{z'} w$ (A.3a)

$$\partial_{t'} \underline{u} + C_2 \nabla' P - \frac{C_3}{Re} \Delta \underline{u} = C_2 \nabla' P - \frac{C_3}{Re} \Delta \underline{u} + \underline{e}_x - \frac{Ri_\tau}{2} T \underline{e}_z + AddNS$$

avec $AddNS = -u \partial_{x'} \underline{u} + [(\epsilon A z' \partial_t f) - w A + u(\epsilon A z' \partial_x f) + \frac{1}{Re} \epsilon A z' (2\epsilon A \{\partial_x f\}^2 - \partial_{x^2} f)] \partial_{z'} \underline{u} - \frac{1}{Re} (2\epsilon A z' \partial_x f) \partial_{z'} \partial_{x'} \underline{u}$

$$+ \frac{1}{Re} \partial_{x'^2} \underline{u} + \frac{1}{Re} (\{\epsilon A z' \partial_x f\}^2 + A^2) \partial_{z'^2} \underline{u} + [-\partial_{x'} P + (\epsilon A z' \partial_x f) \partial_{z'} P] \underline{e}_x - A \partial_{z'} P \underline{e}_z$$
 (A.3b)

$$\partial_{t'} T - \frac{C_4}{Re Pr} \Delta T = - \frac{C_4}{Re Pr} \Delta T + AddHeat$$

avec $AddHeat = -u \partial_{x'} T + [(\epsilon A z' \partial_t f) - w A + u(\epsilon A z' \partial_x f) + \frac{1}{Re} \epsilon A z' (2\epsilon A \{\partial_x f\}^2 - \partial_{x^2} f)] \partial_{z'} T$

$$- \frac{1}{Re} (2\epsilon A z' \partial_x f) \partial_{z'} \partial_{x'} T + \frac{1}{Re} \partial_{x'^2} T + \frac{1}{Re} (\{\epsilon A z' \partial_x f\}^2 + A^2) \partial_{z'^2} T$$
 (A.3c)

Actually, this method permits to stabilise the calculation by maximising the number of linear terms on the left side of the equations while reducing the weight of non linear terms on the right side of the equations. We made a sweep on C_1, C_2, C_3, C_4 to see in what extent those terms helped the programs by comparing the program of the [Part 1](#) and the one of [Part 2](#) with $\delta = 0$. When we take C_1, C_2, C_3, C_4 too low the program has difficulty not to diverge. When we take them too high, the effect of non linearity are a little blurred. A good set is to take $C_1 = C_2 = 10, C_3 = C_4 = 100$, we fix them like that for the rest of the simulations.

A.4 Decomposition test

In hopes of improving program convergence while decreasing resolution, we have tried to decompose speed and temperature into two terms:

$$\underline{u} = \underline{u}_p + \underline{u}_v \quad (A.4a)$$

$$T = T_p + T_v \quad (A.4b)$$

\underline{u}_v (T_v) brings the difference in speed (temperature) between the speed (temperature) of the flow and that of the stationary solution. However the result was opposite to the one expected. The simulations were, for the same resolution, more efficient using the equations on \underline{u} rather than on \underline{u}_v . The reason for this discrepancy would be due to the fact that the \underline{u}_v system would be much more sensitive to the slightest variation.

A.5 Asymptotic expansion of the boundary condition

A lighter method than domain remapping was first tested. The principle is to study the non-planar problem in the case of infinitesimal perturbation. We then perform an asymptotic expansion of the boundaries conditions [equations \(2.2\)](#), as follows

$$\underline{u}(z = h + \delta(x, t)) = 0 \quad (\text{A.5a})$$

$$= \underline{u}(z = h) + \partial_z \underline{u}(z = h)\delta(x, t) + o(\delta^2) \quad (\text{A.5b})$$

$$T(z = h + \delta(x, t)) = 0 \quad (\text{A.5c})$$

$$= T(z = h) + \partial_z T(z = h)\delta(x, t) + o(\delta^2) \quad (\text{A.5d})$$

The equations dictating the dynamics of the system are then unchanged, only the boundary conditions are, as follows to order one:

$$\underline{u}(z = h) = -\partial_z \underline{u}(z = h)\delta(x, t) \quad (\text{A.6a})$$

$$T(z = h) = -\partial_z T(z = h)\delta(x, t) \quad (\text{A.6b})$$

Therefore, we carried out a few simulations with this formalism, but since domain remapping was working, we did not longer on this method. Nevertheless, it remains an interesting method to verify the results given by domain remapping in the case of small perturbations. Due to lack of time we did not do this.

A.6 Importance of checking

In order to have a first verification phase of the program with the domain remapping, we carried out a series of comparison tests between the simulations of [PART 1](#) and the simulations of [PART 2](#) in the case of a zero topography, *ie* $\delta(x, t) = 0$. The similarities between the results allowed us to start in the use and interpretation of the domain remapping simulations in a confident way. This step was important because it allowed us to think on several numerical points about the implementation of domain remapping. But this step also revealed a writing error in the implementation of the equations in *Dedalus*. Indeed, the domain remapping equations being a bit heavy, it is likely to make a mistake when implementing them in *Dedalus*.